High-Resolution SPECT Imaging of Stimuli-Responsive Soft Microrobots

Journal Article

Author(s):
Iacovacci, Veronica; Blanc, Alain; Huang, Henwei; Ricotti, Leonardo; Schibli, Roger; Menciassi, Arianna; Behe, Martin; Pané, Salvador; Nelson, Bradley [iD]

High-resolution SPECT imaging of stimuli-responsive soft microrobots

Veronica Iacovacci*, Alain Blanc, Henwei Huang, Leonardo Ricotti, Roger Schibli, Arianna Menciassi, Martin Behe, Salvador Pané*, and Bradley J. Nelson

Dr. V. Iacovacci, Dr. Henwei Huang, Dr. Salvador Pané, Prof. B.J. Nelson
Institute of Robotics and Intelligent Systems
ETH Zurich, Zurich, CH-8092, Switzerland
E-mail: viacovac@ethz.ch, veronica.iacovacci@santannapisa.it, vidalp@ethz.ch

A. Blanc, Prof. Roger, Schibli Dr. M. Behe
Center for Radiopharmaceutical Sciences
Paul Scherrer Institut, Villigen, CH5232, Switzerland

Dr. Veronica Iacovacci, Prof. L. Ricotti, Prof. A. Menciassi
The BioRobotics Institute
Scuola Superiore Sant'Anna, Pisa, 50126, Italy

Abstract

Untethered small-scale robots have great potential for biomedical applications. However, critical barriers to effective translation of these miniaturized machines into clinical practice exist. High resolution tracking and imaging *in vivo* is one of the barriers that limit the use of micro- and nanorobots in clinical applications. Here, the inclusion of radioactive compounds in soft thermoresponsive magnetic microrobots is investigated to enable their SPECT imaging. Four microrobotic platforms differing in hydrogel structure and four ^{99m}Tc[Tc]-based radioactive compounds are investigated in order to achieve optimal contrast agent retention and optimal imaging. Single microrobot imaging of structures as low as 100 μm in diameter, as well as the tracking of shape switching from tubular to planar configurations by inclusion of ^{99m}Tc[Tc] colloid in the hydrogel structure are reported.

Manuscript

Wireless micro- and nanoscale robots are miniaturized structures with the ability to perform tasks under the application of external power sources [1], or by harvesting reagents available in their surroundings [2, 3]. One of the ultimate goals of these devices is to perform biomedical tasks such as microsurgery or targeted drug delivery in confined locations of the human body [4, 5]. The issues of locomotion in biologically relevant fluids [6] and the release of therapeutic payloads [7-9] are currently in focus. Preliminary work with animal models has recently shown the potential of small-scale robots in the biomedical field [10-12]. While much progress has been made during the last decade, several key issues remain unsolved, and work on the development of biocompatible (either biodegradable [13, 14] or retrievable [15]) and "visible" microrobots [16] is still required. One of the most challenging issues that prevents the translation of small-scale machines to the clinic is the lack of strategies for the effective tracking of these devices during their journey in the human body [17, 18]. A synergistic development of diverse research areas including chemical functionalization of the surface of micro- and nanostructures with contrast agents and advanced imaging technologies is key for further development of untethered small-scale robots for *in-vivo* application [16]. Advancements in microrobot imaging have been recorded. Nelson and coworkers have shown that a swarm of magnetic helical micromachines functionalized with dyes could be tracked *in vivo* in the peritoneal cavity of a mouse using Near Infra-Red (NIR) imaging, while simultaneously maneuvering them using rotating magnetic fields [19]. Recently, Sanchez's group has succeeded in monitoring populations of catalytic micromotors by positron emission tomography [20] whereas Guan and co-workers demonstrated the tracking of autonomous nanomotors through fluorescence [21]. The tracking of magnetic microrobots moving through the abdominal aorta of a mini-pig using X-rays has been demonstrated by Park and coworkers [22]. Misra's group capitalized on ultrasound to follow the position of self-propelled

microparticles [23]. Martel's group [24], and more recently, Zhang and coworkers [25], have used magnetic resonance imaging (MRI) to track the position of magnetic microrobots in small animals. However to date, none of these reports have achieved single microrobot imaging with the ability to detect changes in microrobot configuration. Most clinical imaging techniques employed for microrobot tracking rely on contrasting the magnetic or acoustic properties of the surrounding tissue, making it difficult to determine microstructures in certain parts of the body. This work investigates the inclusion of an imaging agent, which can guarantee successful imaging independent of the properties of the surrounding tissue.

In addition to tracking problems, microrobot structural materials must be carefully considered for their biocompatibility, retrieval potential, or degradation properties. A current trend in small-scale robotics is the replacement of hard components with soft–bodied building blocks. The use of soft materials in these devices brings several advantages, such as a safe interaction with biological environments, more articulated locomotion mechanisms, and in many cases, enhanced biocompatibility and biodegradability. Among the wide selection of soft materials available, hydrogels are promising candidates for building blocks of soft small-scale robots. Hydrogels can react upon external stimuli by changing their morphology, through solubilizing or degrading [26]. Their chemistry can also be tailored to interact favorably with cells and tissues [27, 28]. In addition, the physicochemical constitution of hydrogels allows these materials to host different kinds of compounds in their matrix, ranging from drugs, magnetic nanoparticles and electrically conductive nanorods, to fluorescent dyes, contrast agents or radioactive tracers [29]. The versatility of hydrogels enables the construction of highly integrated micro- and nanorobotic platforms with multiple functionalities. An interesting family of hydrogels that has recently been developed in microrobotics are thermally responsive magnetic nanocomposites. These gels can be remotely controlled using magnetic fields to reach a target location, or to induce a shape transition. These morphological changes are used to modulate their dynamic behavior [30] or to release therapeutic agents [31, 32].

This study presents for the first time, a magnetically driven theranostic soft microrobot made of a thermally responsive hydrogel bilayer. The micromachine contains magnetic nanoparticles and a radioactive compound acting as an imaging agent in its hydrogel frame. The magnetic nanoparticles can be used to remotely drive the locomotion and the shape transformation of the microdevice (by activating the thermoresponsive gel), while the imaging agent allows the microrobot to be monitored *in vivo*.

The proposed soft microrobot can also transport drugs to be released on demand (see supplementary information, Figure S2 and Figure S3). A radioactive compound placed in the microrobot body allows the device to be monitored with high spatial resolution using different tomographic imaging techniques. The chassis of the microrobot consists of two layers: (*i*) a thermoresponsive layer (made of N-isopropylacrylamide (NIPAAM), acrylamide (AAM), poly(ethyleneglycol) diacrylate (PEGDA), 2,2-dimethoxy-2 phenylacetophenone and ethyl lactate (EL)) in which magnetic nanoparticles are embedded, and (*ii*) a supporting layer (made of PEGDA) doped with ^{99m}Tc[Tc] to enable single-photon emission computed tomography (SPECT) imaging of the microrobot (Figure 1 A). The different swelling behavior of the two layers once immersed in water allows the transition from an initial planar configuration to a tubular geometry at body temperature. Shape switching (back to the unfolded planar configuration) can be activated through thermal stimuli (above 42°C) triggered by NIR stimuli. Microrobots were fabricated according to a previously reported protocol based on two photolithography steps, as illustrated in Figure 1B.
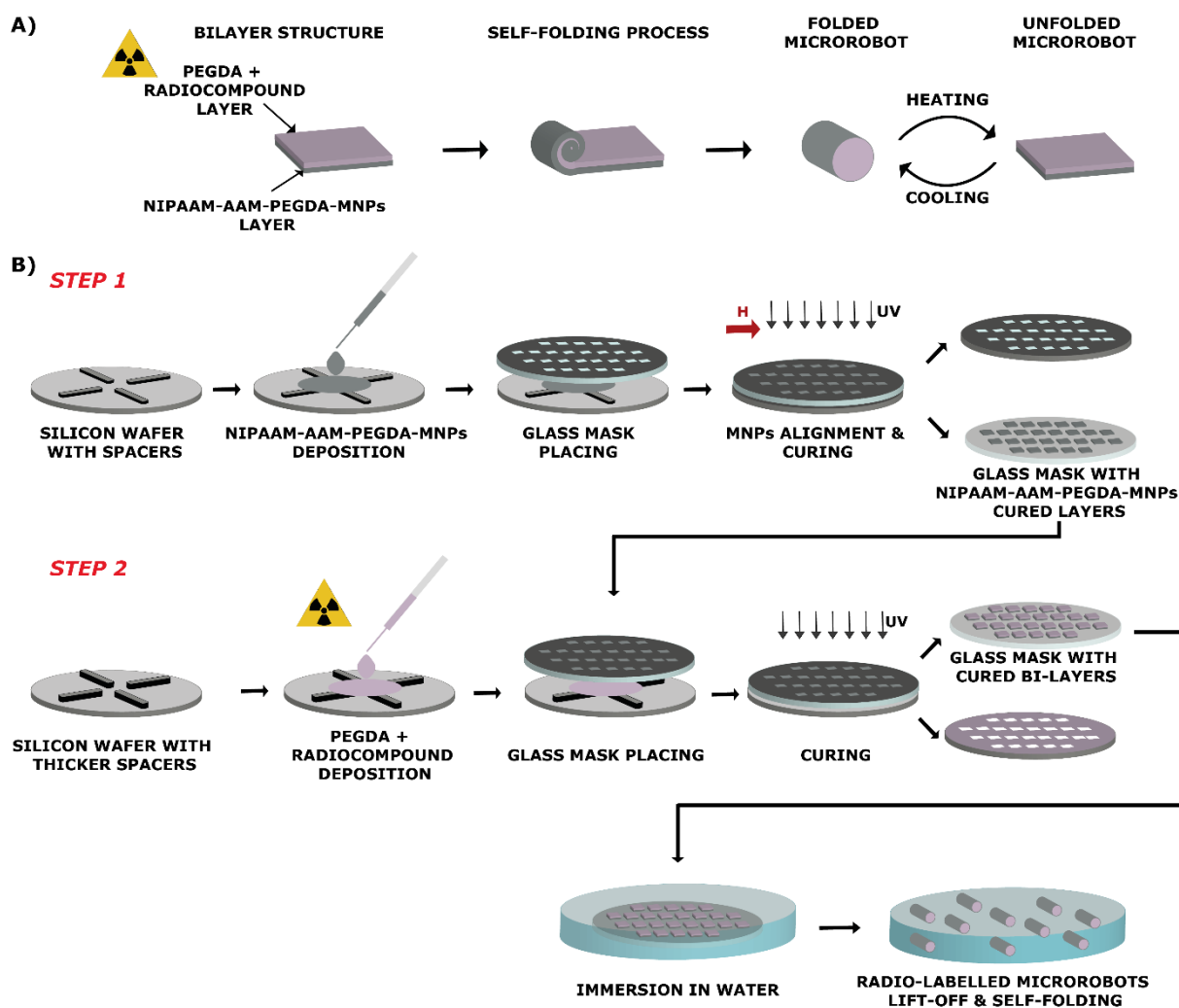
Figure 1 Fabrication workflow of shape-switching theranostic soft microrobots. A) Bilayer structure and self-folding mechanism enabling to obtain tubular microrobots able to undergo a shape switching from the folded (tubular) to the unfolded (planar) configuration, due to a change in the thermoresponsive layer swelling state, upon temperature increase. B) Two-steps photolithography fabrication process with inclusion of a radioactive compound in the supporting PEGDA layer.

We screened different microrobots of varying dimensions and types of ^{99m}Tc[Tc] radioactive compound base. Two-dimensional square hydrogel bilayer structures with side lengths of 3, 1.5, 1 and 0.5 mm (thicknesses are reported in Table S1) were successfully produced. SPECT is a medical imaging technique that is based on conventional nuclear medical imaging and tomographic reconstruction methods. The technique requires the delivery of a gamma-emitting radioisotope (a radionuclide) such as ^{99m}Tc- or ^{111}In-based compounds into the patient, normally through injection into the bloodstream. The image device is typically a scintillation camera system which includes a lead collimator and photomultiplier tubes to convert γ-ray photons into

an electric signal. 3D radioactivity distribution is assessed by combining projection images acquired through 360° rotations of the scintillation camera. In this work, a 4-head multiplexing multi-pinhole camera (NanoSPECT/CTplus, Bioscan Inc., Poway, CA, USA) was used to enable high resolution estimation of three-dimensional radioactivity distribution (

Figure *2* A) . The advantage of SPECT is that the γ-rays source is contained within the body and radiation dose is extremely limited when dealing with radio-emitting microrobots. A significant decrease in the absorbed radiation dose can be witnessed in comparison to levels from X-ray computed tomography (CT), which employs an external X-ray source that performs a 360° rotation together with the detector to record the body's anatomy (e.g. SPECT effective dose is 2.5 mSv against the 8 of abdominal CT).

In this study, Technetium-99m (^{99m}Tc[Tc], $t_{1/2}$ = 6 h) was selected for use as the radioisotope as it can easily form ^{99m}Tc[Tc]-based compounds. Four different ^{99m}Tc[Tc]-based compounds were investigated as contrast agents. Pertechnetate (TcO_4^-; 99Mo/99mTc generator, Mallinckrodt, Petten, The Netherlands), neurotensin-His-tag ^{99m}Tc[Tc]-tricarbonyl nuclide (Nuclide) [33, 34], ^{99m}Tc[Tc] colloid (Nanocolloid) and ^{99m}Tc[Tc]-Exametazim (d,l-hexamethylpropylenaminoxim) (d,l HMPAO; ROTOP Pharmaka GmbH Dresden Germany) were employed as imaging agents and included in the PEGDA solution at a 30% v/v concentration, prior to the polymerization process. This concentration was optimal for imaging, and did not compromise the hydrogel polymerization.

The initial stage was to assess the ability of the hydrogel to retain the imaging agent in its matrix. The microrobots were then washed to remove the surface excess of radioactive compound. The spontaneous release in a phosphate buffer solution (PBS) at room temperature was evaluated for 2 hours through a gamma counter for 0.5, 1.5 and 3 mm microrobots in the folded configuration. This time interval was considered relevant in relation to clinical procedures. Hydrogel microrobots containing TcO_4^- exhibited a release of 90% of the contrast agent in the first five minutes (results not shown), and subsequently a residual radioactivity below the

sensitivity of SPECT (that avoided microrobots imaging). In this situation, the release of TcO_4^- was expected due to its ionic nature and tendency to diffuse from the hydrogel matrix. Radioactive compound release was lower in the three remaining cases with $^{99m}Tc[Tc]$ nanocolloid giving the optimal inclusion in the microrobot structure, with a residual radioactivity between 80 and 95% on microrobot dimensions (

Figure *2* B). The residual radioactivity for ^{99m}Tc-based HMPO and the nuclide was always below 50% and 28% respectively. Suboptimal inclusion resulted in an unwanted imaging agent release that could hamper microrobot tracking through SPECT. This release could create a radioactivity distribution in areas dissociated from the microrobot itself. A poor retention implies a low residual radioactivity, which results in low quality imaging, especially at smaller dimensions, corresponding to a smaller volume of the doped hydrogel.
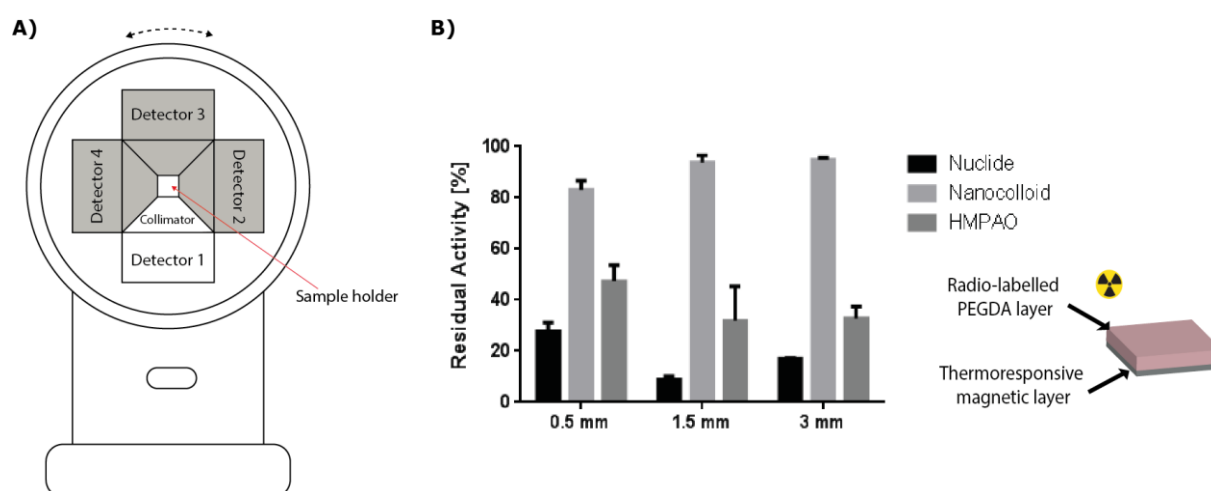

Figure 2 A) Schematization of a 4-head multiplexing multi-pinhole camera SPECT system. B) Microrobot residual radioactivity after 2 h of incubation at room temperature for different radioactive compounds and microrobots dimension.

Next, the feasibility of performing SPECT imaging of soft microrobots with different dimensions and configuration (folded and unfolded states) was assessed. Image reconstruction and registration among CT and SPECT images confirmed microrobot identification. Both SPECT and CT images were recorded from different cutting planes: coronal, sagittal and transversal. As expected, hydrogel microrobots doped with HMPAO and Nuclide were not well

resolved by SPECT due to a weak retention of the imaging agent by the hydrogel matrix. In these cases, only hydrogels with a size of 3 mm could be identified due to their relatively high volume, incorporating more radioactive compound (Figure 3).
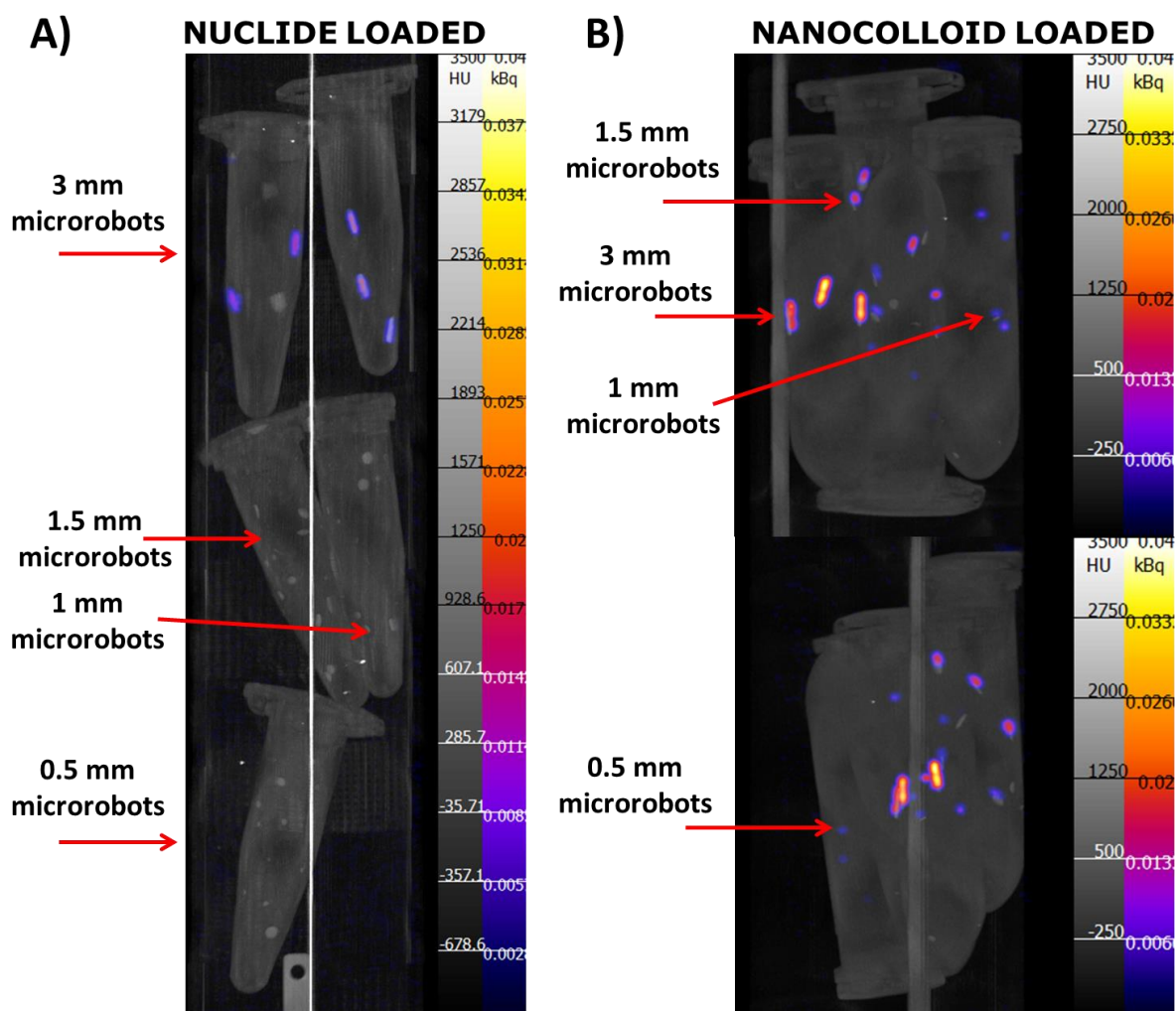

Figure 3 SPECT imaging of 3mm, 1.5 mm, 1 mm and 0.5 mm microrobots embedding ^{99m}Tc[Tc]- radionuclide (A) and ^{99m}Tc colloid (B). In both the images the same color scale has been employed.

However, ^{99m}Tc[Tc] colloid-doped microrobots could be resolved using SPECT, for all dimensions (down to 0.5 mm) and in both configurations (folded and unfolded). This was due to a better retention of the colloid nanoparticles by the hydrogel matrix, in comparison to the other radioactive compounds tested. Figure 4A (second row) shows that it is possible to image a tubular hydrogel microrobot with a length of 500 µm and a diameter of 100 µm. We also ran CT images for comparison along the same cutting planes (Figure 4 A-D, first row) to ensure

that the radioactivity distribution detected by SPECT corresponded to the microrobots, and not to free or released radionuclide which had been dispersed in the medium. CT imaging was enabled by magnetic nanoparticles inclusion, but is used here only as comparison. We also used SPECT on a 3 mm microrobot to assess the feasibility of detecting a change in the morphological configuration. Figure 4E shows that SPECT was able to identify the morphological transformation of the microrobot from the unfolded (planar) to the folded (tubular) configuration. This reinforces the suitability of the proposed clinical imaging technique to track soft microrobots and to detect their shape transformation. Shape change could be used as a triggering mechanism for drug release activation and for modulating locomotion performance. Comparison between SPECT and optical microscope images revealed that in addition of being able to detect shape transformation, SPECT provides accurate microrobots images which accuracy in representing microrobots shape and features appears comparable even to bright field optical microscopy (Figure S5).

After successful imaging of the hydrogel microrobots, we also performed imaging *ex vivo*. Microrobots with different dimensions and doped with ^{99m}Tc[Tc] colloid were injected ex-vivo in the intraperitoneal cavity of a mouse. A SPECT acquisition (of 540 minutes duration) was performed after the implantation, which showed that microrobots can be clearly detected in the mouse abdomen, both in the sagittal and coronal views.
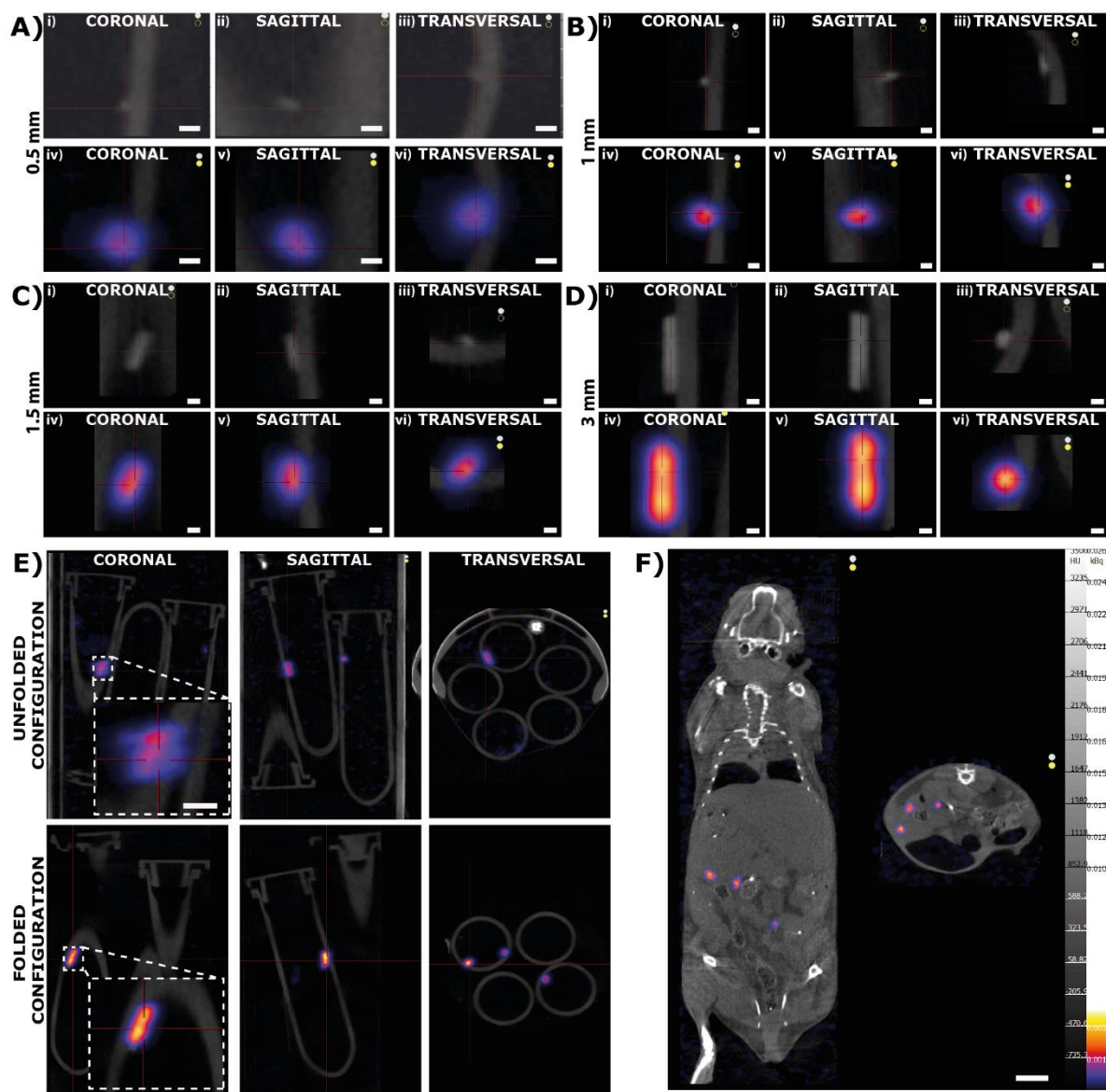
Figure 4 CT and SPECT imaging of the theranostic microrobots loaded with ^{99m}Tc nanocolloid. A-D) CT and SPECT imaging of a single 0.5 mm (A), 1 mm (B), 1.5 mm (C) and 3 mm (D) microrobot. For each microrobot dimension, projections along the three main cutting planes are reported (scale bar 500 μm). E) In vitro 3 mm microrobot SPECT images in the folded and unfolded configurations along the three main cutting planes. This result demonstrates the ability to use this imaging technique to track microrobot shape transition (scale bar 2 mm). F) Ex vivo imaging of radiolabelled microrobots subcutaneously injected in mice. Images along the sagittal and coronal cutting plane are reported (scale bar 10 mm).

Conclusions

Although in-body high resolution imaging is undoubtedly crucial for future successful employment of microrobots in clinical practice, this method needs more research. The use of medical imaging strategies for microrobot position tracking and for verifying the successful performance of a therapeutic function (*e.g.* shape transition, to enable drug release) would speed up the clinical translation of these miniaturized machines. This study demonstrates that it is

10

possible to load soft shape-switching microrobots with ^{99m}Tc[Tc]-based imaging agents and to efficiently view them through SPECT, both *in vitro* and *ex vivo*, for different microrobot dimensions and configurations. The study also shows for the first time, that it is possible to perform single microrobot imaging when using hydrogel structures as low as 100 μm in diameter. The results of this report represent a significant step forward for future development in the field of single-robot closed-loop control and activation, leading to the innovative and clinically feasible medical application of microrobots.

EXPERIMENTAL SECTION

Microrobots Fabrication

N-Isopropylacrylamide monomer (NIPAAM), Acrylamide (AAM), Poly(ethyleneglycol) diacrylate (average MW 575, PEGDA), 2,2-dimethoxy-2 phenylacetophenone (99%, DMPA) and Ethyl Lactate (98%, EL) employed in microrobot fabrication were purchased from Sigma Aldrich. NIPAAM-AAM-PEGDA (molar ratio 85/15/1) solution, with 3 wt% DMPA photoinitiator and 70 wt% EL, was used for the thermoresponsive layer production. 1 wt% silica-coated γ-Fe_2O_3 nanoparticles was added and dispersed into the solution by ultrasonication. The amounts of AAM and crosslinking agent (PEGDA) to be embedded in the hydrogel structure were selected to achieve a lower critical solution temperature (LCST) of around 42°C, with a suitable swelling ratio.

The microrobots were the result of a two-step, backside exposure, photolithographic process (Figure 1 B), where the two different layers were created on a glass photo mask, without alignment. The thickness of the layers was controlled using an SU-8 spacer which was previously fabricated on silicon wafers using standard photolithography. To prevent adhesion of the hydrogels, a non-adhesive layer was evaporated onto spacer substrates through an overnight silanization process and then activated at 90°C. Glass masks allowed the microrobots to achieve the desired 2D shape which was obtained by standard photolithography using a positive photoresist (AZ4562). A 100 nm chromium layer was evaporated onto the glass substrates and then removed from the featured areas by rinsing the photoresist with acetone and isopropanol. The two different layers were fabricated in sequence. The first step involved the use of a NIPAAM-AAM-PEGDA-MNP solution deposition on a silicon substrate provided with SU-8 spacers, with particle alignment under an unidirectional magnetic field, and UV polymerization on the glass mask to obtain monolayer square robots (under a 365 nm UV lamp for 60 s).

After separating the two substrates, the cured NIPAAM-AAM-PEGDA layer remained attached to the mask side which allowed us to proceed with the second step. To add the supporting layer, the PEGDA+RADIOACTIVE COMPOUND/DRUG solution was deposited on a thicker spacer substrate before mask placement. Polymerization was carried out for an additional 90 seconds under UV light. (365 nm). After curing, the bilayers attached to the mask were released through immersion in water.

The same fabrication process was employed to obtain microrobots of different dimensions (in the range 0.5 – 3 mm of side) by varying the glass mask pattern and the SU-8 spacer thickness (Table S1). For imaging tests and radioactive compound inclusion, the microrobot fabrication process was carried out according to the established protocol in a glovebox and with an optimized overflow to avoid radioactive contamination.

Microrobot Imaging

$TcO4^-$ (pertechnetate) was obtained by $^{99m}Tc[Tc]$ elution in saline solution. Nuclide solution was obtained by labeling $^{99m}Tc[Tc]$ in its stable oxidation state, namely ^{99m}Tc-tricarbonyl, with Neurotensin by using inverted Histidine (His-tag) as a binding ligand. The binding produced more stable molecules which allowed a better embedding in the polymeric matrix. A metallic reducing agent, Zinc, was used to obtain colloidal pertechnetate dispersion by reducing TcO_4^- to a lower oxidation state. Zinc chloride ($ZnCl_2$, Sigma Aldrich) was added to the TcO_4^- solution at a concentration of 4 mg/ml to obtain a $^{99m}Tc[Tc]$ colloid. A ^{99m}Tc-Exametazim (d,l-Hexamethyl-propylenaminoxim) kit (ROTOP Pharmaka GmbH), typically employed for SPECT brain imaging, was used to obtain HMPO and to test the behavior of a lipophilic compound.

In all cases, the radioactive compound release was evaluated for 0.5, 1.5 and 3 mm microrobots over 2 hours. Microrobots that had previously undergone a washing process aimed at removing the residual radioactive compound were placed on the microrobot external surface and were

incubated at room temperature in 1 mL of PBS in order to test the spontaneous release. 20 µL samples were collected from the incubation medium at 5, 15, 30, 60, 90 and 120 minute intervals. At the end of the test, the microrobots were collected from the incubation medium in order to measure their residual radioactivity. The radioactivity in all the collected samples was measured using a Gamma counter. The release profiles were not reproducible for all the tested compounds, due to a high inhomogeneity in the incubation solution and to the nonlinear release kinetics (data not shown).

Radioactive microrobots of various dimensions were placed in Eppendorf tubes. CT/SPECT imaging was performed through a CT-Nano SPECT equipped with a 1 mm diameter pinhole aperture (Ref: NSP-108-M14-WB). Image reconstruction and registration among CT and SPECT images, aimed at superimposing the two sets of data to prove microrobot identification (and to distinguish them from accidental radioactive compound droplets), were achieved using the manufacturers HiSPECT software. Image processing and interpretation was performed using the VivoQuant (inviCRO, Boston, MA) software.

Supporting Information

Supporting Information is available from the Wiley Online Library or from the author.

S1. Bilayer microrobots dimensioning and optical imaging

Layer thickness could be properly determined based on the swelling properties of the bilayer

components and on tube dimensions. As a rule of thumb, the highest swelling ratio layer, the

NIPPAM-AAM-PEGDA, should have a thickness (t_1) equal to around 1/100 of the square side,

whereas the supporting layer thickness should be about one third of the thickness of the first

layer. Table S1 shows the spacer thickness associated with the different 2D square dimensions:

t_1 refers to the thickness of the thermoresponsive layer and t_2 represents the overall microrobot

thickness (thermoresponsive layer thickness + supporting layer thickness). The proposed

fabrication process was successful for all the tested dimensions with the reported layer thickness.

SQUARE SIDE	t_1	t_2
3 mm	30 µm	45 µm
1.5 mm	6 µm	10 µm
1 mm	6 µm	10 µm
0.5 mm	4 µm	6 µm

Table S 1. Hydrogel layers thickness at varying of 2D side dimensions.

Figure S1 shows microrobots optical images when varying dimensions (according to Table S1)
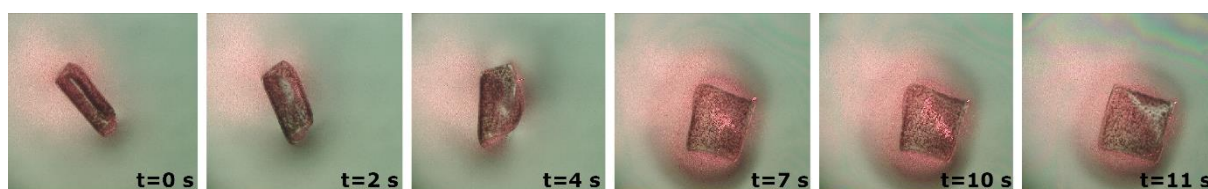
and configuration (folded versus unfolded).
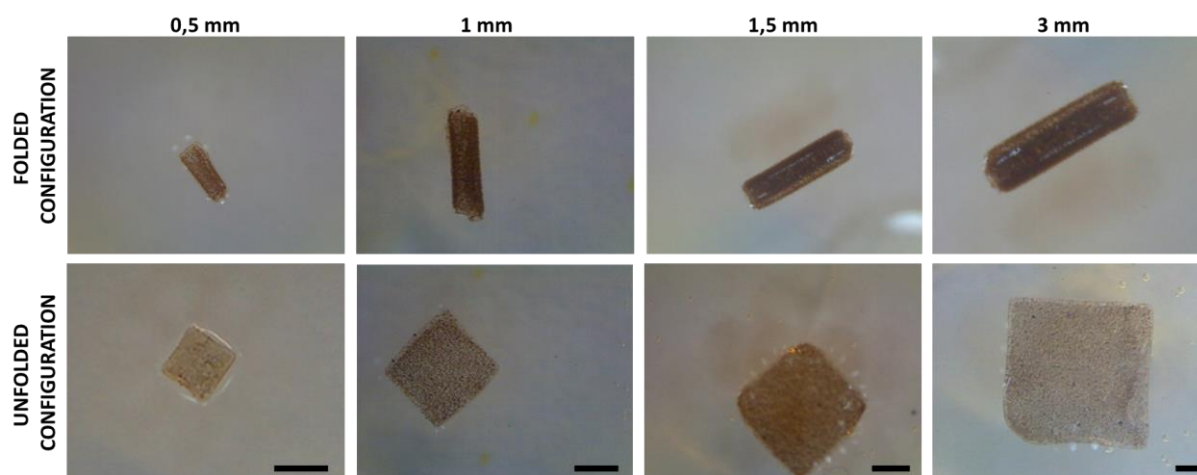
Figure S 1 Microrobot optical images at dimensions and configuration varying (scale bar 0.5 mm).

S2. NIR light triggered shape transition

Microrobots responsiveness to NIR was also tested to verify that the energy transferred by the laser and converted into heat on absorbance by the embedded MNPs was sufficient to enable structural heating and shape transition even with reduced dimensions. NIR stimulation was performed by placing a 785 nm laser (power 1.5 W, laser spot intensity 7.64 W/cm^2) at a distance of approximately 7 cm from the microrobot, in compliance with the anatomical distances in a common *in vivo* environment. The average response time required by the microrobots to unfold upon irradiation was measured in seconds (Figure S 2).

Figure S 2. NIR induced shape transition from the folded to the unfolded configuration for a 0.5 mm microrobot.

S3. Triggered drug release tests

We have also demonstrated the possibility of including a model drug, in this instance doxorubicin, into the supporting layer of the fabricated microrobot. The aim was to use the shape transition from the folded to the unfolded configuration, activated upon temperature increase, to expose the drug loaded layer and to trigger drug release. As opposed to previously reported works in which the entire structure was loaded with a drug, the inclusion of the therapeutic compound in only one of the two polymeric layers, the inner PEGDA, allows a significant increase in drug release due to the shape transition and to the exposure of the drug loaded layer to the surrounding fluids. The tubular shape of the folded structure can limit spontaneous drug diffusion during the journey of the microrobot to its target location, minimizing interaction with the surrounding fluids. The drug loaded layer can only be exposed to diffusion by applying a triggering stimulus which induces shape transition and drug release. We have demonstrated that changing the shape of these microrobots maximizes their drug delivery function. It is worth noting that also the temperature increase itself contributes to a

faster release kinetics due to an increase in the diffusion coefficient, thus furtherly enhancing drug release upon NIR-mediated thermal stimuli.

A doxorubicin hydrochloride (Sigma Aldrich, 44583) aqueous solution (10 mg/mL) was added to the PEGDA solution to achieve an overall 1 mg/mL drug concentration. Once a homogeneous doxorubicin-PEGDA solution was obtained under sonication, microrobots were fabricated according to the protocol described in the experimental section.

Drug release was evaluated over a 24 hour period. In order to test the effects of shape changing, drug release tests were carried out by incubating the microrobots in d-H_2O both at room temperature and at 43°C, which is above the thermoresponsive layer LCST temperature (in order to induce shape transition). Cumulative doxorubicin release was evaluated by collecting the incubation medium at specific intervals (every hour for the first six hours and then 24 hours after incubation), replacing it with fresh d-H_2O (kept at the relative incubation temperature) to approximate a perfect sink condition. The level of doxorubicin released by the microrobots was measured using a UV-vis spectroscopy (Infinite M200 Pro, Tecan AG, Mannendorf, Switzerland) by setting an excitation wavelength of 470 nm and an emission wavelength of 585 nm. Absorbance data was processed based on the drug calibration curve previously obtained, where aqueous doxorubicin solutions showing different concentrations (in the range of 0-30 μg/mL) were prepared, and absorbance measures were carried out on 300 μL samples in triplicate for each concentration. The drug calibration curve was then drawn using the absorbance data. In the first part of the calibration curve, where the doxorubicin concentrations were relative to low, the trend could be approximated to linear and this was then used to derive the amount of doxorubicin released by each microrobot,

Doxorubicin release tests were repeated in triplicate under the same experimental conditions for microrobots with side dimensions of 0.5, 1, 1.5 and 3mm, and in both the folded and unfolded configuration. It is evident that shape switching significantly enhances drug delivery

in all four tested dimensions, and that spontaneous drug delivery is very low in the folded configuration, particularly during short term release.

We have also demonstrated that the temporal release profile can be reproduced across the four tested dimensions, and that with the exception of the 1 mm samples where a high variability in the amount of drug release was recorded, drug release efficiency increases with shape switching and with decreasing dimensions. 500 μm microrobots released 90% of the embedded drug on triggering compared to 22% in the other configurations. This behavior is even more evident by normalizing the drug release in the unfolded configuration to the volume of the drug loaded layer (Figure S3): release efficiency significantly increases with decreasing dimensions, confirming the need to translate the proposed therapeutic microrobotic paradigm to the microscale.
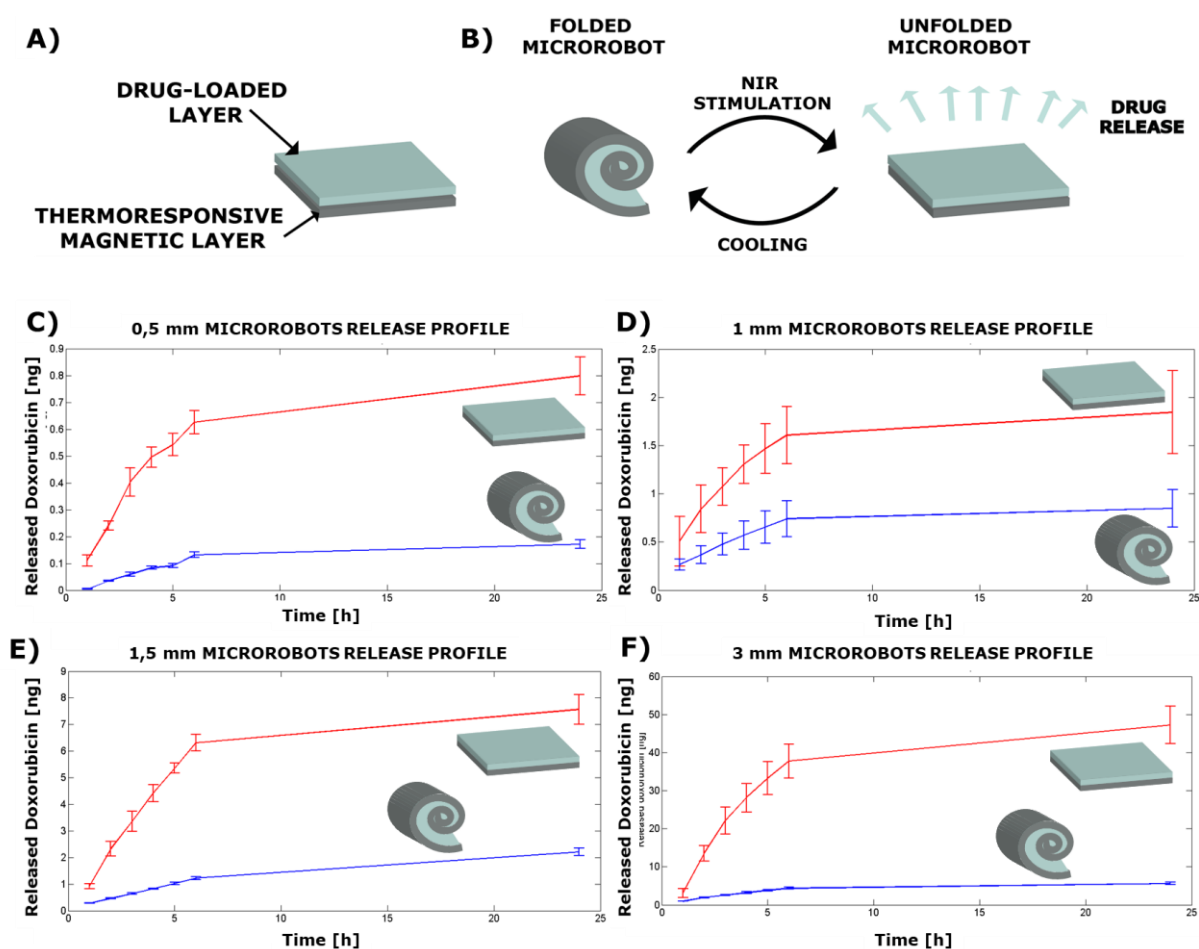
Figure S 3. Triggered drug release: A) depiction of the bilayer structure; B) representation of the microrobot shape transition due to NIR triggering and the drug release mechanism; C-F) cumulative drug release profiles for different microrobot dimensions in the folded and unfolded configurations.
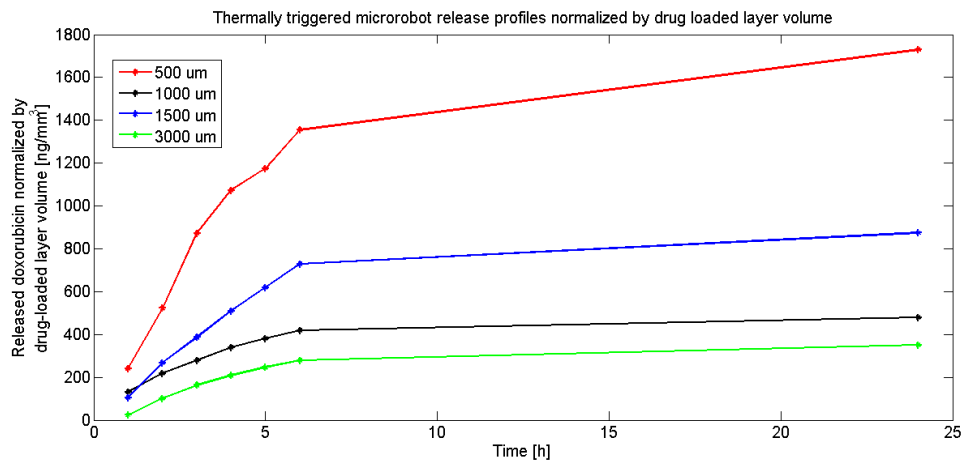
Figure S 4. Doxorubicin release in the unfolded configuration across the four dimensions, normalized to the volume of the drug loaded hydrogel layer.

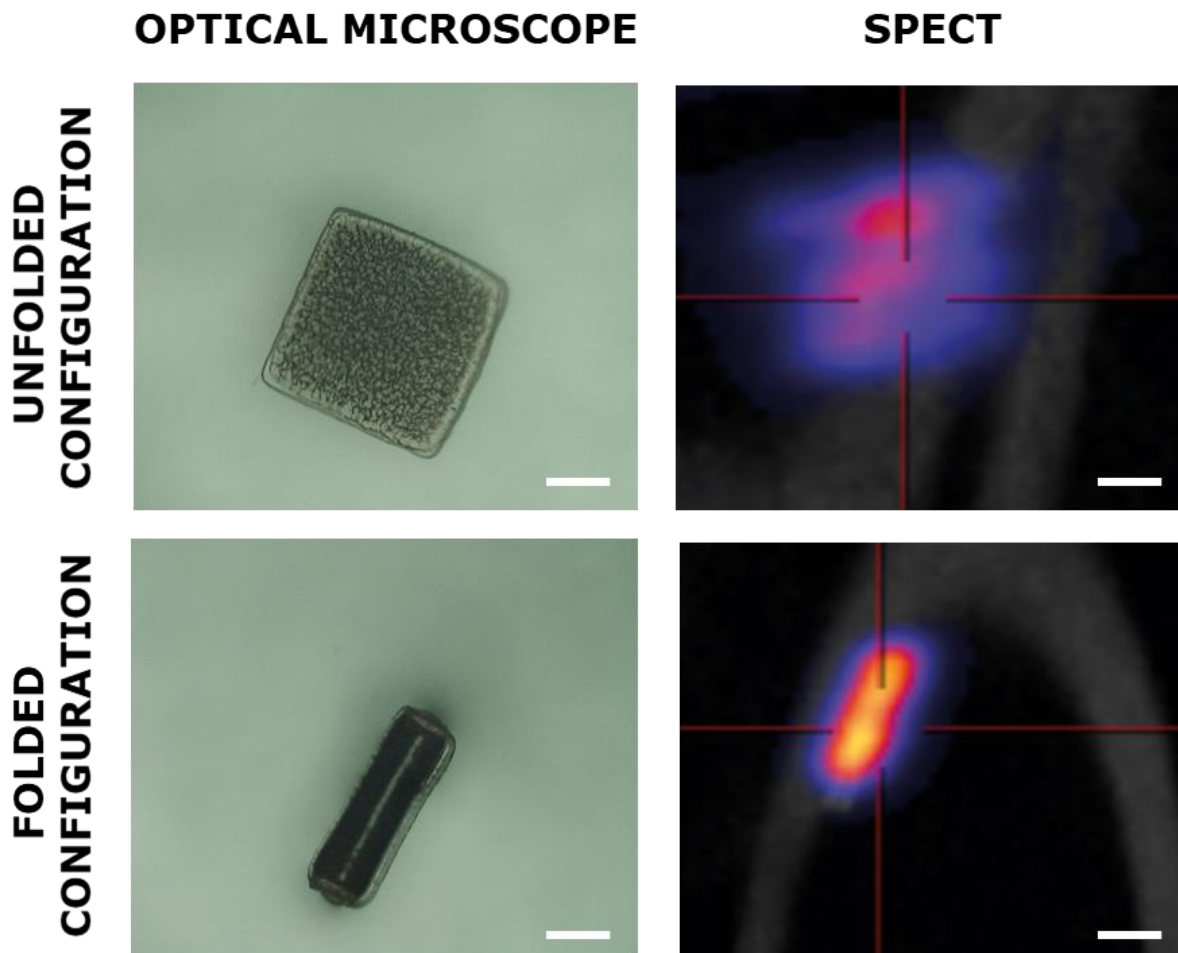## S5. Comparison between optical and SPECT imaging.

Figure S 5 Comparison between optical microscope and SPECT images of a 3 mm microrobot bot in the folded and unfolded configuration (scale bar 1 mm).

References

1.   Tottori, S.; Nelson, B. J., *Small* **2018**, 1800722.
2.   Hu, C.; Pané, S.; Nelson, B. J., *Annual Review of Control, Robotics, and Autonomous Systems* **2018,** *1*, 53-75.
3.   Chen, X. Z.; Jang, B.; Ahmed, D.; Hu, C.; De Marco, C.; Hoop, M.; Mushtaq, F.; Nelson, B. J.; Pané, S., *Advanced Materials* **2018,** *30* (15), 1705061.
4.   Li, J.; de Ávila, B. E.-F.; Gao, W.; Zhang, L.; Wang, J., *Science Robotics* **2017,** *2* (4), eaam6431.
5.   Ornes, S., *Proceedings of the National Academy of Sciences* **2017,** *114* (47), 12356-12358. DOI 10.1073/pnas.1716034114.
6.   Yu, J.; Zhang, L., *IEEE/ASME Transactions on Mechatronics* **2018**.
7.   Srivastava, S. K.; Clergeaud, G.; Andresen, T. L.; Boisen, A., *Advanced drug delivery reviews* **2018**.
8.   Luo, M.; Feng, Y.; Wang, T.; Guan, J., *Advanced Functional Materials* **2018**, 1706100.
9.   Iacovacci, V.; Lucarini, G.; Ricotti, L.; Dario, P.; Dupont, P. E.; Menciassi, A., *Biomedical microdevices* **2015,** *17* (3), 63.
10.   Hoop, M.; Ribeiro, A. S.; Rösch, D.; Weinand, P.; Mendes, N.; Mushtaq, F.; Chen, X. Z.; Shen, Y.; Pujante, C. F.; Puigmartí‐Luis, J., *Advanced Functional Materials* **2018**, 1705920.
11.   de Ávila, B. E.-F.; Angsantikul, P.; Li, J.; Lopez-Ramirez, M. A.; Ramírez-Herrera, D. E.; Thamphiwatana, S.; Chen, C.; Delezuk, J.; Samakapiruk, R.; Ramez, V., *Nature communications* **2017,** *8* (1), 272.
12.   Li, J.; Li, X.; Luo, T.; Wang, R.; Liu, C.; Chen, S.; Li, D.; Yue, J.; Cheng, S.-h.; Sun, D., *Science Robotics* **2018,** *3* (19), eaat8829.
13.   Wang, X.; Qin, X. H.; Hu, C.; Terzopoulou, A.; Chen, X. Z.; Huang, T. Y.; Maniura‐Weber, K.; Pané, S.; Nelson, B. J., *Advanced Functional Materials* **2018**, 1804107.
14.   Bozuyuk, U.; Yasa, O.; Yasa, I. C.; Ceylan, H.; Kizilel, S.; Sitti, M., *ACS nano* **2018,** *12* (9), 9617-9625.
15.   Iacovacci, V.; Ricotti, L.; Sinibaldi, E.; Signore, G.; Vistoli, F.; Menciassi, A., *Advanced Science* **2018**, 1800807.
16.   Medina-Sánchez, M.; Schmidt, O. G., *Nature* **2017,** *545*, 25.
17.   Wang, B.; Zhang, Y.; Zhang, L., *Quantitative imaging in medicine and surgery* **2018,** *8* (5), 461.
18.   Pané, S.; Puigmartí‐Luis, J.; Bergeles, C.; Chen, X. Z.; Pellicer, E.; Sort, J.; Počepcová, V.; Ferreira, A.; Nelson, B. J., *Advanced Materials Technologies*, 1800575.
19.   Servant, A.; Qiu, F.; Mazza, M.; Kostarelos, K.; Nelson, B. J., *Advanced Materials* **2015,** *27* (19), 2981-2988.
20.   Vilela, D.; Cossío, U.; Parmar, J.; Martínez-Villacorta, A. M.; Gómez-Vallejo, V.; Llop, J.; Sanchez, S., *ACS nano* **2018,** *12* (2), 1220-1227.
21.   Mou, F.; Chen, C.; Zhong, Q.; Yin, Y.; Ma, H.; Guan, J., *ACS applied materials & interfaces* **2014,** *6* (12), 9897-9903.
22.   Park, S.; Cha, K.; Park, J., *International Journal of Advanced Robotic Systems* **2010,** *7* (1), 1.
23.   Khalil, I. S.; Ferreira, P.; Eleutério, R.; de Korte, C. L.; Misra, S. In *Magnetic-based closed-loop control of paramagnetic microparticles using ultrasound feedback*, Robotics and Automation (ICRA), 2014 IEEE International Conference on, IEEE: **2014**; pp 3807-3812.

24.   Pouponneau, P.; Soulez, G.; Beaudoin, G.; Leroux, J.-C.; Martel, S., *Cardiovascular and interventional radiology* **2014,** *37* (3), 784-790.
25.   Yan, X.; Zhou, Q.; Vincent, M.; Deng, Y.; Yu, J.; Xu, J.; Xu, T.; Tang, T.; Bian, L.; Wang, Y.-X. J., *Sci. Robot* **2017,** *2* (12).
26.   Peppas, N. A.; Hilt, J. Z.; Khademhosseini, A.; Langer, R., *Advanced materials* **2006,** *18* (11), 1345-1360.
27.   Trel'ová, D. a.; Salgarella, A. R.; Ricotti, L.; Giudetti, G.; Cutrone, A.; Šrámková, P.; Zahoranova, A.; Chorvát Jr, D. a.; Hasko, D.; Canale, C., *Langmuir* **2018**.
28.   Palagi, S.; Fischer, P., *Nature Reviews Materials* **2018,** *3* (6), 113-124. DOI 10.1038/s41578-018-0016-9.
29.   Liang, G.; Yang, Z.; Zhang, R.; Li, L.; Fan, Y.; Kuang, Y.; Gao, Y.; Wang, T.; Lu, W. W.; Xu, B., *Langmuir* **2009,** *25* (15), 8419-8422.
30.   Huang, H.-W.; Sakar, M. S.; Petruska, A. J.; Pané, S.; Nelson, B. J., *Nature Communications* **2016,** *7*, 12263. DOI 10.1038/ncomms12263
http://www.nature.com/articles/ncomms12263#supplementary-information.
31.   Fusco, S.; Sakar, M. S.; Kennedy, S.; Peters, C.; Bottani, R.; Starsich, F.; Mao, A.; Sotiriou, G. A.; Pané, S.; Pratsinis, S. E.; Mooney, D.; Nelson, B. J., *Advanced Materials* **2014,** *26* (6), 952-957. DOI 10.1002/adma.201304098.
32.   Malachowski, K.; Breger, J.; Kwag, H. R.; Wang, M. O.; Fisher, J. P.; Selaru, F. M.; Gracias, D. H., *Angewandte Chemie* **2014,** *126* (31), 8183-8187.
33.   Badar, A.; Williams, J.; de Rosales, R. T.; Tavaré, R.; Kampmeier, F.; Blower, P. J.; Mullen, G. E., *EJNMMI research* **2014,** *4* (1), 14.
34.   Egli, A.; Alberto, R.; Tannahill, L.; Schibli, R.; Abram, U.; Schaffland, A.; Waibel, R.; Tourwé, D.; Jeannin, L.; Iterbeke, K., *Journal of Nuclear Medicine* **1999,** *40* (11), 1913-1917.